Available online at www.sciencedirect.com

SCIENCE DIRECT®

Vision Research 45 (2005) 2352–2366

Vision Research

www.elsevier.com/locate/visres

Refractive index distribution and optical properties of the isolated human lens measured using magnetic resonance imaging (MRI)

C.E. Jones [a], D.A. Atchison [b], R. Meder [a], J.M. Pope [a,*]

[a] School of Physical and Chemical Sciences, Queensland University of Technology, GPO Box 2434, 2 George St., Brisbane 4001, Australia
[b] School of Optometry, Queensland University of Technology, GPO Box 2434, Brisbane 4001, Australia

Received 23 June 2004; received in revised form 12 October 2004

Abstract

Using a non-invasive MRI technique for measuring the refractive index distribution through the crystalline lens, refractive index maps were obtained through 20 intact isolated human lenses (7–82 years). Focal length measurements, obtained by simulated light ray propagation through each index map were found to be in agreement with direct measurements performed on a scanning laser apparatus. With increasing age, the refractive index profiles became flatter in the central region, accompanied by steepening of the profile in the periphery. This appears to be an important mechanism underlying the observed changes in power and longitudinal aberration of the human lens.

Keywords: Eye lens; Lens optics; Refractive index distribution; Gradient index; Magnetic resonance imaging

1. Introduction

Attempts to measure the refractive index distribution through the human crystalline lens to date have usually either been invasive or have invoked assumptions about the shape of the distribution and/or of the iso-indical contours. Measurements of the refractive index distribution through the lens are known to go back over a century to Matthiessen (1880), who took discrete measurements using an Abbe refractometer. Measurements have also been performed by freezing and slicing the lens (Nakao, Fujimoto, Nagata, & Iwata, 1968) or measuring protein content (Fagerholm, Philipson, & Lindström, 1981). By adapting a ray tracing technique for measuring the refractive index distribution through fibre optic preforms with a circular (Chu, 1977) or elliptical (Barrell & Pask, 1978) cross-section, Campbell (1984) non-destructively measured the refractive index distribution through the isolated rat lens, which is ellipsoidal in shape. This technique also required the lens to be surrounded by a medium whose refractive index matched the index at the edge of the lens. In a study of bovine lenses, Chan, Ennis, Pierscionek, and Smith (1988) modified the ray tracing technique so that index matching was not necessary, but the method assumed the lens to have a circular cross-section and axial (radial) symmetry in the plane of simulation so that the refractive index distribution was only measured in the equatorial plane and then transposed to the sagittal plane on the assumption that the shape of the distribution (when expressed as a function of normalised radius), was the same in both sagittal and equatorial planes. Modelling the isoindical contours as a family of concentric bi-ellipses, Pierscionek, Chan, Ennis, Smith, and Augusteyn (1988) applied this method to isolated bovine and also

* Corresponding author. Tel.: +61 7 3864 2325; fax: +61 7 3864 1804.
E-mail address: j.pope@qut.edu.au (J.M. Pope).

0042-6989/$ - see front matter © 2005 Elsevier Ltd. All rights reserved.
doi:10.1016/j.visres.2005.03.008

human lenses. Again they measured refractive index distribution in the equatorial plane and then transposed the distribution to the sagittal plane. While the refractive index distribution in the sagittal plane could be verified by laser ray tracing for the bovine lenses, results were not consistent with predictions of the fitted index distribution for human lenses, suggesting that the assumption that the shape of the distribution is the same in both equatorial and sagittal planes may not be valid for human lenses. Using a reflectometric fibre optic sensor, Pierscionek (1997) directly measured refractive index along the equatorial and sagittal planes and concluded that the normalised profiles along the two planes did not coincide. Acosta et al. (2002) have developed a tomographic method for measurement of the refractive index profile. This technique requires radial symmetry of the index distribution and also requires ray paths to be approximated by parabolas. Barbero, Glasser, Clark, and Marcos (2004) have developed a technique based on global optimisation algorithms. It was concluded that this method required realistic assumptions about the form of the index distribution to be effective.

In summary, the more direct, invasive methods of measuring refractive index distribution employed to date suffer from the disadvantage that they may affect the measured refractive index. In most cases (Abbe refractometer, fibre optic probe) they are also discrete and probably not capable of measurement with sufficient resolution to determine the continuous two or three dimensional distribution of refractive index in the human lens. Non-invasive measurements on the isolated lens (involving laser ray tracing) generally assume the refractive index distribution to conform to a particular model, whereas in practice the human lens appears to deviate from such simple models.

In vivo determinations of the crystalline lens index distribution have been performed by Pomerantzeff, Pankratov, Wang, and Dufault (1984). They performed calculations based on measurements of spherical aberration and of the curvatures and intra-ocular spacing of human eyes. Again however, no direct measurements of refractive index were performed. It has been observed by Pierscionek and Chan (1989) that this approach produces one of a range of possible index distributions that would produce the same spherical aberration curve and does not result in a unique solution. Al-Ahdali and Messiery (1995) also performed in vivo determinations based on optical performance of the eye rather than direct index measurements. This technique was also based on an assumed model of the index distribution. Roth and Kluxen (1990) captured refraction of a laser beam through the crystalline lens in vivo with a Scheimpflug camera. Although the index distribution was not constrained to a particular model the crystalline lens was compartmentalised into lamellae and the refractive index of each lamella calculated sequentially using Snell's law. The resulting index distributions did not resemble direct measurements of protein concentration distribution (Fagerholm et al., 1981) or model independent measurements of refractive index distribution (Moffat, Atchison, & Pope, 2002a, 2002b) through human lenses.

There is a need for a schematic model of the eye that includes a model lens based on reliable measurements of its refractive index distribution. Further, the models most often used, such as the Gullstrand eye (see e.g. Atchison & Smith, 2000), are not complete because the lens only exists in one or two accommodative states (relaxed and fully accommodated). A complete model of the eye would include a lens with accurately modelled geometry, refractive index distribution and age-dependent accommodative amplitude, as well as a description of the continuous changes in lenticular geometry and index distribution that occur with both age and accommodation. The lens is the ocular component whose changes are most pronounced with age, and it is also the only component that changes with accommodation. It follows that the observed changes in power and aberrations of the eye with age and accommodation can be better understood with an accurately modelled lens. Schematic eyes are used as the theoretical basis in the development for surgical techniques such as LASIK and intraocular implantation (Atchison & Smith, 2000) that are becoming increasingly popular. Therefore an updated schematic eye with an accurately described lens is timely not only to refine the development of such techniques, but also to predict the effect of such surgery on the aberrations of the eye that are known to change with age (Artal, Berrio, Guirao, & Piers, 2002; Smith, Cox, Calver, & Garner, 2001) and level of accommodation (Cheng et al., 2004; Glasser & Campbell, 1998). An improved understanding of the refractive index distribution of the lens and how it changes with age and accommodation would also aid the development of intraocular implants by more clearly defining what we wished to emulate. Such knowledge would also be useful for more precisely measuring dimensions of features on the retina, as its image captured with a fundus camera will have been distorted by the crystalline lens and the cornea. Similarly, as suggested by Roth and Kluxen (1990), improved modelling of the lens and measurement of its index distribution could be used to construct a fundus camera for imaging the entire retina. Improved understanding of the index distribution of the crystalline lens would also have applications in interferometric imaging, such as optical coherence tomography. The dimensions of interferometric images are those of optical path length which is dependent on refractive index as well as geometrical distance. Therefore intraocular dimensions could be measured more accurately with improved knowledge of the refractive index distribution of the crystalline lens.

In this study the refractive index distribution through the isolated human eye lens was measured non-invasively and age-dependent trends in the distribution were examined, using a novel magnetic resonance imaging (MRI) technique developed in our laboratory (Moffat et al., 2002a, Moffat, Atchison, & Pope, 2002b). The basis of this new method is the finding that both a standard MRI measurable parameter, the transverse or spin–spin relaxation time T_2, (or its reciprocal, $R_2 = 1/T_2$), and the local refractive index value are dependent on the concentration of macromolecules (notably crystalline proteins) in the lens tissue (Jones & Pope, 2004). The eye lens has a protein concentration distribution (Fagerholm et al., 1981), which is responsible for determining the optical density and hence the refractive index distribution. The transverse relaxation rate R_2 also depends on protein concentration because of the ability of proteins to act as relaxation sites for water protons. As in our previous study of porcine lenses (Jones & Pope, 2004), the R_2 distribution was measured in the form of discrete 2-dimensional R_2 maps. By empirically determining the dependence of refractive index on R_2, the R_2 maps were converted to refractive index maps. The optical properties of the lens were then determined by simulating the propagation of light rays through the refractive index maps using Snell's law to calculate surface refraction and a standard ray tracing algorithm for gradient index media (Sharma, Kumar, & Ghatak, 1982). The experimentally acquired refractive index maps were then verified by directly measuring the focal length of each lens using a scanning laser apparatus.

2. Methods

In our preliminary study (Moffat et al., 2002a, 2002b), due to limited supply of human lens tissues, the empirically determined calibration curve for converting R_2 maps to refractive index maps was rudimentary (only 7 data points) and the refractive index maps were not verified optically, lenticular paraxial power being estimated using a model dependent technique (Atchison & Smith, 1995). Using the methods discussed in Sections 2.2 and 2.3 below, a more accurate calibration curve was obtained (30 data points), from lens tissue derived from 66 isolated human lenses and the full longitudinal aberration curves were obtained by simulated ray tracing through the refractive index maps of 20 isolated lenses. The focal lengths were then also measured directly using a scanning laser apparatus as described in Section 2.4.

2.1. Materials

MRI and scanning laser experiments were carried out on 20 intact human lenses. These methods have been discussed in detail previously (Jones & Pope, 2004). All MRI measurements were made at 34.5 °C in artificial aqueous humour (AAH). The AAH was prepared in sterile conditions from: Minimum Essential Medium Eagle medium (9.4 g l^{-1}) with Earle's salts (MEM) (Sigma M-0769 Sigma-Aldrich, Castle Hill, NSW) and L-Glutamine (2 mM), Penicillin (1 mgl^{-1}), Streptomycin (1 mg l^{-1}) solution (Sigma G-1146), with the addition of amphotericin B (10 mg/l), buffered with HEPES (Sigma H-7523) (2.38 g/l) and adjusted with NaOH to a pH of 7.4. For the scanning laser experiments, lenses were immersed in a saline solution similar to that used in a previous optical study on isolated lenses (Vilupuru & Glasser, 2001), consisting of: $NaH_2PO_4 \cdot H_2O$ (0.1 g/l), KCl (0.4 g/l), NaCl (8 g/l), sucrose (1 g/l), buffered with HEPES (2.38 g/l) and adjusted with NaOH to a pH of 7.4. Human eye lenses were purchased from the Queensland Eye Bank. After excision at the eye bank, lenses were stored at room temperature in sterile conditions in AAH. In the laboratory, lenses were stored at 34 °C until required for measurement. Measurements on intact human lenses were performed between 2 and 5 days post-mortem.

2.2. Refractive index versus R_2 calibration

Following measurements on the 20 (9 paired and 2 unpaired) intact lenses (discussed in Sections 2.3 and 2.4 below), these lenses were frozen until sufficient lens tissue was available for bulk measurements. An additional 46 human lenses were also purchased, immediately frozen at approximately −20 °C, and used solely for bulk measurements on lens tissue. The data from bulk measurements were used to empirically determine the dependence of refractive index on R_2. The lenses were defrosted at room temperature, de-capsulated and homogenised with a spatula. The mixture was gradually dehydrated at room temperature while samples were removed for calibration measurements. The mixture was then gradually diluted with drops of AAH and samples again removed for calibration purposes. This process ensured the data spanned the range of refractive index distributions expected in the eye lens. Each sample of human lens homogenate was placed in a 5 mm NMR tube and gently centrifuged to transfer the viscous sample to the bottom of the tube. Data for water proton (^{1}H) R_2 measurements were acquired on a Bruker Avance 200 MHz (4.7 T) NMR spectrometer using a standard (spectroscopic) Carr Purcell Meiboom Gill (CPMG) pulse sequence (Carr & Purcell, 1954; Meiboom & Gill, 1958) with an echo spacing of 1 ms. Because the diffusion of water molecules in the imaging gradients can potentially cause an imaging R_2 estimate to be larger than the spectroscopic R_2 value, for 19 of the homogenate samples an R_2 value was also estimated using the same multi-echo imaging pulse sequence used

to acquire R_2 data for the intact lenses. The homogenate sample was then removed from the tube and its refractive index (corresponding to a wavelength of 589 nm) was measured in an Abbe refractometer.

2.3. MRI experiments

Intact human lenses were placed in a 10 mm or 15 mm NMR tube (depending on the diameter of the lens) containing AAH solution. The tube was sealed with a PTFE vortex plug and cap and left to equilibrate in the NMR magnet at a temperature of 34.5 °C for 20 min. The measurements were performed using a standard multi-spin echo imaging sequence (Bruker ParaVision®) on a Bruker Avance 200 MHz NMR imaging spectrometer. The echo spacing was 4.075 ms and 64 echoes were acquired. The image matrix size was 128×128, the field of view was $10 \times 10\ \text{mm}^2$ or $15 \times 15\ \text{mm}^2$ depending of the diameter of the tube, the repetition time TR was 2 s, the slice thickness 1 mm and the number of averages was 16. The R_2 map was obtained by fitting pixel image intensity, S, acquired at echo time, TE, to a single exponential decay: $S = S_0\exp(-R_2 \times \text{TE})$. The subsequent R_2 map was converted to a refractive index map (corresponding to a wavelength of 589 nm) using the equation ascertained from the refractive index versus R_2 calibration. Pixels corresponding to the lens surface were identified by thresholding the refractive index map, beginning with a value of 1.350 and increasing this threshold value in increments of 0.001, until the resulting binary image displayed a clear silhouette of the lens (the intensities of the pixels corresponding to the surrounding AAH being less than the threshold value). Because of noise some pixels in the refractive index map, which clearly did not correspond to the lens, had intensities higher than the threshold values. The coordinates of these pixels were recorded with mouse clicks and not included in the surface data array. The coordinates of the pixels corresponding to the anterior and posterior surfaces of the lens were fitted to semi-ellipses using a non-linear regression algorithm. Because pixels corresponding to the surface of the lens contained signal due to both lens tissue and the surrounding AAH (partial volume artefact), the surface refractive index was estimated by linear extrapolation of the refractive index values near the periphery of the lens to the lens surface. This was achieved by increasing the threshold value of the index map in increments of 0.001 so that iso-indical contours were identified in the same way as the surface contours, and their coordinates fitted to semi-ellipses. The distance of the anterior refractive index contour from the anterior surface contour was calculated as the distance between their intersections with the optical axis. The index value of the contour was calculated by taking the mean of the refractive index values of each pixel lying on the contour. The subsequent refractive index data, n, versus anterior distance from surface, d_a, was fitted to a straight line. By extrapolating this line to $d_a = 0$, the surface refractive index was estimated. Further details are given in Jones and Pope (2004).

The refraction of light rays at the lens surfaces was simulated using Snell's Law, where the surface normals were calculated from the fitted anterior and posterior semi-ellipses. The surrounding medium was assigned the refractive index value of the saline solution used in the scanning laser apparatus (1.340). The refraction of light rays through the gradient of refractive index (GRIN) of the lens was simulated using a standard algorithm for ray tracing through gradient index media (Sharma et al., 1982), which requires index gradients (first order partial differentials) with respect to each spatial coordinate. The two index gradient maps corresponding to the two spatial coordinates of the refractive index map were calculated with the Matlab function "gradient.m'. To increase the effective resolution of the index and gradient maps, a linear interpolation function (Matlab function interp2.m) was implemented during the simulated ray trace. Because laser beams were incident parallel to the optical axis onto the posterior surface of the lens in the scanning laser apparatus (for the reason discussed below), the light rays were also arranged to be incident in this manner for the simulated ray trace through the refractive index map.

2.4. Scanning laser experiments

A schematic diagram of the scanning laser set up is shown in Fig. 1. The isolated lens was placed on a pedestal in a parallel-sided glass tank filled with the buffered saline solution, to which several drops of milk were added to enhance light scattering. The more rounded posterior surface of the lens faced downward, as the relatively flat anterior surface was obscured by the pedestal when it faced downward. An image of the lens was captured with an Electrim EDC-1000E computer camera (Electrim Corporation, Princeton, New Jersey). The pixels corresponding to the lens surface were identified

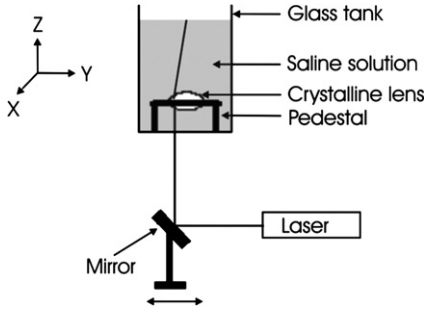

Fig. 1. Schematic diagram of the scanning laser apparatus.

using the edge detection function "edge.m" with the Canny edge-finding method available in the Matlab image processing toolbox. This function returned a binary image with "edge" pixels having an intensity of one and "non-edge" pixels having an intensity of zero. Pixels corresponding to the surface of the lens could be easily be identified from the binary image, however many pixels that did not correspond to the surface of the lens were also given intensities of one. These pixels were assigned intensities of zero by opening the binary image in a commercial image processing program (Paint Shop Pro, Jasc Software, MN, USA) and using the eraser brush to give these pixels the intensity of the background. In a manner similar to the MRI experiment, the coordinates of the surface pixels corresponding to the anterior and posterior surface of the lens were fitted to semi-ellipses. The refractive index of the saline solution (1.340) was measured with the Abbe refractometer. Experiments were performed with a Melles Griot 2 mW, 594 nm, Helium Neon laser. A narrow beam from the laser was reflected off a mirror located directly below the tank and passed through the lens. The mirror was mounted on a platform that could be rotated and translated. The mirror was adjusted until the laser beam appeared to pass unrefracted through the centre of the lens. The entrance beam was then translated in 0.1 mm increments, using a micrometer screw attached to the mirror, so that it traversed the region of the lens exposed through the holder, and its refraction digitally captured. The reading on the micrometer screw corresponding to the initial and final position of the entrance beam was recorded. The distance between the initial and final position of the entrance beam was also measured in pixels from their corresponding images. These measurements were used for distance calibration to convert measurements from pixels to millimetres. Linear fits were made to each entrance and exit beam. Data points for the fits were obtained by normalising the pixels in each row of the image with respect to the pixel of highest intensity in that row and thresholding the normalised image with a threshold value of 0.95. The data were weighted according to the normalised intensity of the pixels. Since the entrance beams were parallel, their fits were improved by averaging their fitted slopes, then re-performing the linear regression. The estimated optical axis was the line with slope equal to the slope of the lines fitted to the entrance beams and which passed through the point that produced the minimum sum of square distance from the lines fitted to the exit beams.

2.5. Comparison of focal length and lens geometry estimated using MRI and the scanning laser technique

In comparing results from the MRI and scanning laser experiments, the front focal length for each ray aperture (i.e. the displacement of the entrance ray from the optical axis) was measured as the distance from the anterior vertex (pole) of the lens to the intersection of the corresponding exit ray with the optical axis. The anterior pole was estimated from the intersection of the optical axis with the anterior semi-ellipse fitted to the lens surface. Although focal length is usually measured from the principal plane, for comparison of MRI and scanning laser estimates in this study, it was measured from the pole, because less error is associated with determining the position of the pole than the principal plane. The front focal length of the lens was taken to be the average of the front focal lengths for normalised ray apertures (with respect to the lens equatorial radius) in the range between 0.2 and 0.6 from the optical axis. The central beams with a ray aperture less than 0.2 normalised units were not included because the exit beams were almost parallel with the optical axis resulting in large uncertainties in estimating the focal point. These central errors were more extreme in the scanning laser study than in the simulated ray traces because of the difficulty in precisely aligning the lens axis with the laser beam. A maximum normalised ray aperture of 0.6 was chosen because values outside this range were not observed during the scanning laser experiment as the lens support pedestal prevented these laser beams entering the crystalline lens (see Fig. 1).

The vertex curvatures of the semi-elliptical anterior and posterior surfaces of the lens, C_a and C_p, were calculated using the formulae:

$$C_a = +\frac{A_a}{B_a^2}, \quad C_p = -\frac{A_p}{B_p^2}$$

where A and B are the major and minor axes respectively of the semi-ellipse obtained from a fit to the coordinates of the anterior and posterior surfaces, and the subscripts a and p refer to the anterior and posterior surfaces respectively. Lens thickness, T, was estimated as the distance between pixels with the minimum and maximum coordinate in the direction of the optical axis (z-axis in Fig. 1). Lens diameter was measured as the distance between pixels with the minimum and maximum coordinate in the direction of the equatorial axis (y-axis in Fig. 1). For the scanning laser experiment, an additional image of the lens was captured after moving the camera closer to the tank so that the lens encompassed a larger proportion of the field of view (FOV). After capturing an additional two images of laser beams at the extremities of this FOV, the distance calibration was performed using the method discussed in Section 2.4.

2.6. Contributions of surface and GRIN refraction to paraxial power of the isolated lens

To estimate the paraxial and mean focal lengths from the index maps, ray traces were re-performed with

the entrance rays (parallel to the optical axis) incident onto the anterior surface of the lens. The surrounding medium was assigned a refractive index of 1.336 corresponding to the index of the aqueous and vitreous humour in the Gullstrand schematic eye. The intersection of the entrance and exit rays gave the 'principal points'. In this paper 'principal points' refers to points on the principal plane, rather than the standard definition of principal points that are on the optical axis and conjugate to each other. As before, the intersection of the exit ray with the optical axis gave the focal points. Instead of measuring focal length from each principal point, in order to reduce scatter in the longitudinal aberration curve (focal length versus ray aperture), while at the same time allowing for comparison of our data with those of previous studies, we attempted to estimate the location of the principal plane by a linear fit to the principal points. However the principal points appeared to fall on a curved rather than straight line. Therefore a 'principal curve' (in the form of a second order even polynomial) was fitted to the principal points:

$$y = c_0 + c_2 x^2 \tag{1}$$

where y is the vertical distance in millimetres from the anterior pole and x is the horizontal distance from the optical axis. A second order even polynomial was used because the principal points appeared to be symmetrical about the optical axis, and two coefficients adequately described the curve. In order to estimate paraxial focal length, the ray aperture was normalised with respect to the equatorial radius of the lens and the resulting longitudinal aberration data were fitted to a fourth order even polynomial, and the polynomial evaluated for a ray aperture of zero. Mean focal length was calculated by averaging the focal lengths of all ray apertures for each lens. The following formula was used to convert focal length to power:

$$P = \frac{1000 \times n_{\text{medium}}}{\text{FL}} \tag{2}$$

where P is the power in dioptres, n_{medium} is the refractive index of the medium surrounding the lens (1.336) and FL is the focal length in millimetres.

To measure the contribution of surface refraction to total lens paraxial power, the paraxial surface power was calculated using the thick lens formula:

$$P_{\text{surface}} = P_{\text{a}} + P_{\text{p}} - \frac{T \times P_{\text{a}} \times P_{\text{p}}}{n_{\text{surface}}} \tag{3}$$

where $P_{\text{a}} = C_{\text{a}} \times (n_{\text{surface}} - n_{\text{medium}})$, $P_{\text{p}} = C_{\text{p}} \times (n_{\text{medium}} - n_{\text{surface}})$. P_{surface} is the vertex surface power, P_{a} and P_{p} are the refractive powers of the anterior and posterior surfaces respectively, n_{surface} is the surface index of the lens and n_{medium} is the refractive index of the medium surrounding the lens (1.336).

3. Results

3.1. Refractive index versus R_2 calibration

The refractive index versus (spectroscopic) R_2 data for human lens homogenate samples are illustrated in Fig. 2. The dependence was well described by a second order polynomial:

$$n = 1.3554(\pm 0.0017) + 1.549(\pm 0.072) \times 10^{-3} R_2 - 6.34(\pm 0.65) \times 10^{-6} R_2^2 \tag{4}$$

($R = 0.995$, $p < 0.0001$ (all coefficients)), where n is refractive index and R_2 is in s^{-1}. This is the calibration equation that was used to convert R_2 maps into refractive index maps. In Fig. 3, the imaging R_2 data are plotted against the spectroscopic R_2 data together with the line $y = x$. There appeared to be no significant difference between the two estimates as the data points fell on the line $y = x$ within the limits of their error bars.

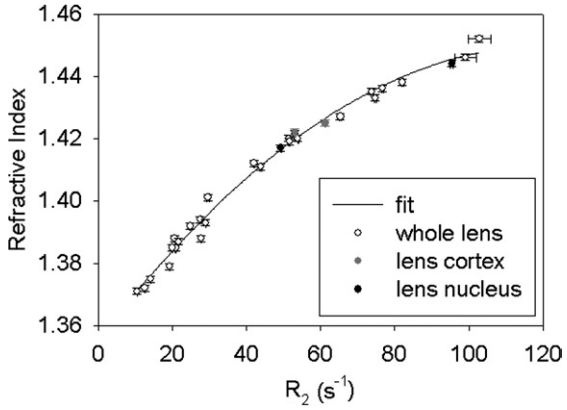

Fig. 2. Dependence of refractive index on R_2 for human lens homogenate samples at 4.7 T and 34.5 °C. The R_2 value was estimated spectroscopically.

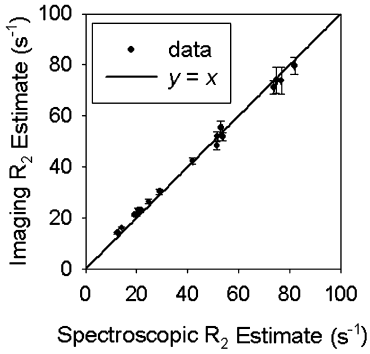

Fig. 3. Comparison of R_2 measured spectroscopically with values obtained using a spin multi-echo imaging sequence. The data are plotted together with the line $y = x$. Error bars (too small to be visible for the spectroscopic measurements) correspond to 95% confidence limits on the non-linear least squares parameter estimate.

3.2. MRI and scanning laser experiments on intact lenses

R_2 maps through each of the 20 lenses were obtained using the method discussed in the previous section, converted to refractive index maps using Eq. (4), then the surface pixels were corrected for the partial volume artefact. Fig. 4(a) shows the refractive index map through the lens of a 40 year old donor. Fig. 4(b) shows the binary image obtained by thresholding the refractive index map. The regions enclosed in grey rectangles were due to noise and were removed with the mouse. The coordinates of the surface pixels are indicated by the grey points. Fig. 4(c) displays the semi-elliptical fits to the surface data of the same lens. Refractive index maps through a 7 and 82 year old lens are shown in Fig. 5, together with refractive index profiles along the optical and equatorial axes. For the older lens, the index profile exhibits a broad flat 'plateau' with a steep gradient at the periphery, while for the younger lens the index profile is more curved. Fig. 6 displays iso-indical contour plots for eight lenses aged from 7 to 82 years. From this figure it is apparent that the increasing flatness of the central region of the index profile, accompanied by a steepening of the profile in the periphery of the lens, occurs gradually with age. Another age-related trend observed in a preliminary MRI study of the isolated human eye lens (Moffat et al., 2002a, 2002b) was that the refractive index at the centre of the lens decreased linearly with age, while the refractive index at the surface displayed no age dependence. Fig. 7 displays the age dependence of the central and surface refractive index values from this study. There was little dependence of central refractive index on age ($R = -0.150$, $p = 0.528$) and no dependence of surface index on age ($R = 2.03 \times 10^{-3}$, $p = 0.993$). The mean and standard deviation of these parameters were:

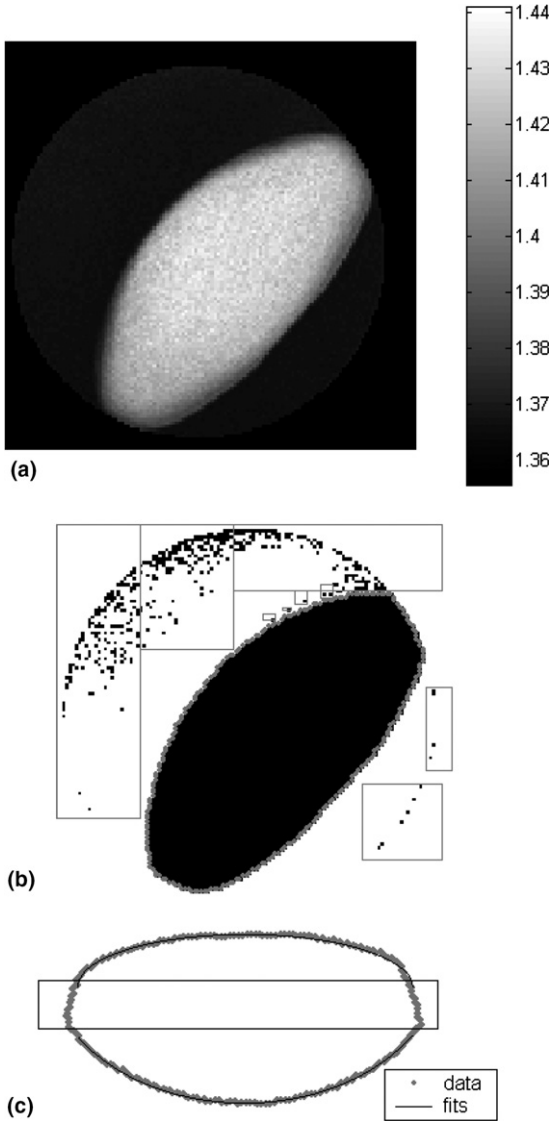

Fig. 4. Identification of lens surface pixels in the MRI experiment. (a) Refractive index map through the lens of a 40 year old donor. (b) Binary image obtained by thresholding the refractive index map. The regions enclosed in grey boxes were due to noise and were removed manually. Coordinates of the surface pixels are indicated by the grey dots. (c) Semi-elliptical fits to the surface coordinate data of the same lens.

$$n_c = 1.4181 \pm 0.075 \quad (5)$$

$$n_s = 1.3709 \pm 0.0039 \quad (6)$$

where n_c is the central refractive index, n_s is the surface refractive index. Fig. 8 shows the results of a simulated ray trace through a 35 year old lens. The solid dots indicate the 'principal points' of the lens where the extrapolated entrance and exit rays intersect. The open circles indicate the longitudinal aberration data i.e. the horizontal coordinate indicates the ray aperture (displacement of the incident ray from the optical axis) and the vertical coordinate is that of the focal point where the exit ray intersects the optical axis.

Fig. 9 illustrates edge detection and surface fitting in the scanning laser experiment for the same lens shown in Fig. 4 for the MRI experiment. Fig. 9(a) displays the captured lens profile. Fig. 9(b) displays the corresponding binary image obtained using the method discussed in Section 2.4. Fig. 9(c) displays the semi-elliptical fits to the edge data. Fig. 10 illustrates linear fits to the entrance and exit beams using the method discussed in Section 2.4. Fig. 10(a) shows an image generated by superimposing the captured refraction of three beams in the scanning laser experiment. Fig. 10(b) illustrates linear fits to the data points of these beams and the semi-elliptical fit to the top surface profile of the lens. Fig. 10(c) displays the linear fits together with the image of a single refracted beam. In the scanning laser experiment the range of aperture values was restricted by the pedestal used to support the lens.

Fig. 11 compares the longitudinal aberration curves obtained from the MRI and scanning laser experiments

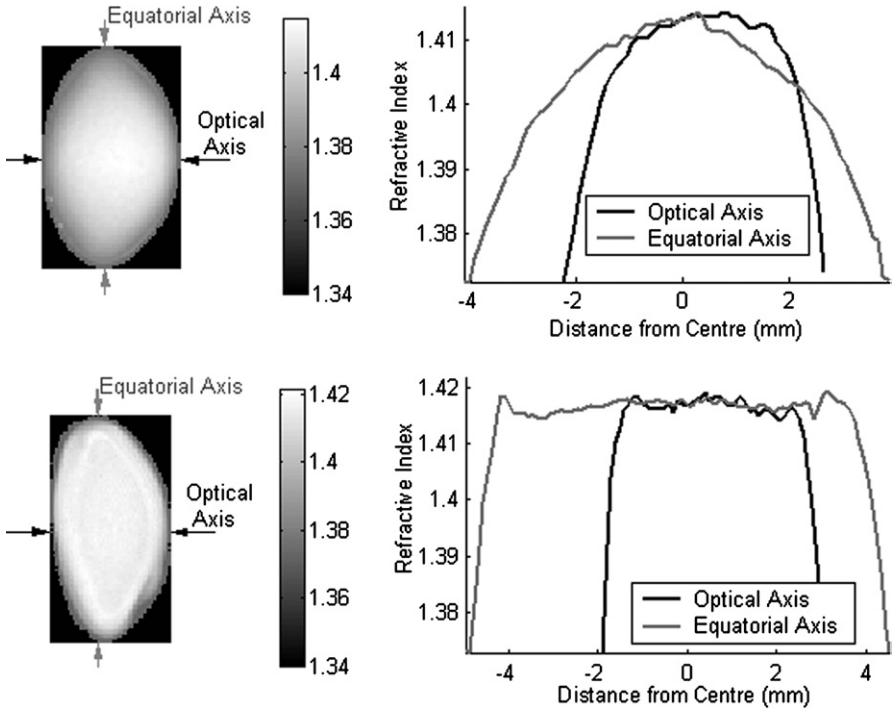

Fig. 5. Refractive index maps (left) and profiles (right) through 7 year old (upper) and 82 year old (lower) lenses. The lens centre was taken to be the intersection of the optical and equatorial axes, selected by a mouse click using the cursor cross-hairs.

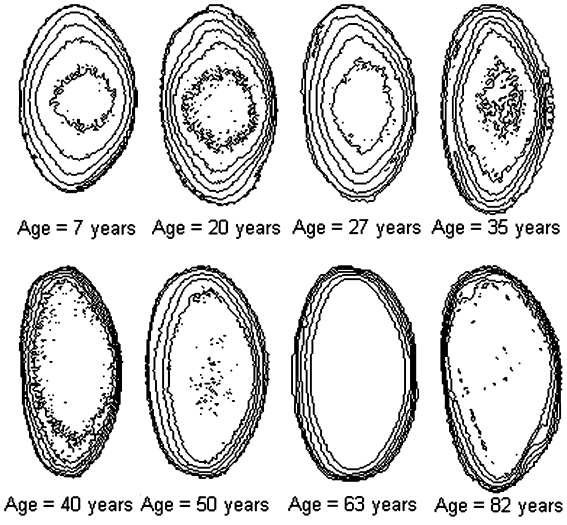

Fig. 6. Iso-indical contour plots obtained from refractive index maps through human lenses aged 7–82 years. For clarity the index values of the contours, ranging from 1.36 to 1.43 in increments of 0.01 (corresponding to just below the surface values to just above the central values) have been omitted from the maps.

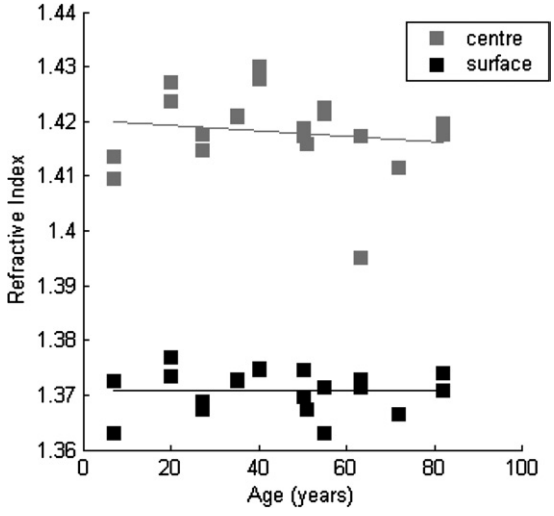

Fig. 7. Central and surface refractive index (wavelength = 589 nm) of the human eye lens versus age of donor. Results of linear regressions were: $n_c = 1.4204(\pm 0.0039) - 5.1(\pm 7.9) \times 10^{-5} \times \text{Age}$ ($R = 0.150$, $p = 0.528$); $n_s = 1.3709(\pm 0.0020) - 3(\pm 400) \times 10^{-7} \times \text{Age}$ ($R = 2.03 \times 10^{-3}$, $p = 0.993$).

for the same lens. In this figure the ray aperture has been normalised with respect to the equatorial radius of the lens. The age-dependence of the front focal length, anterior and posterior vertex curvatures, equatorial diameter and thickness measured using the two techniques are summarised in Table 1 and Figs. 12–14. The intercepts and slopes of the regression lines of the five parameters (front focal length, anterior and posterior vertex curvature, thickness and diameter) measured using the MRI technique and the scanning laser apparatus were found to not be significantly different ($p > 0.5$ for all slopes and intercepts apart from the slope for anterior curvature where $p = 0.35$) based on a test using the t-statistic (see e.g. Zar, 1984).

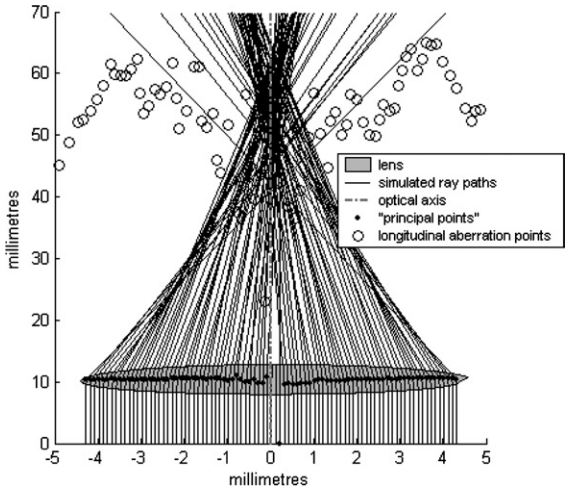

Fig. 8. Result of a ray trace through the refractive index map of a 35 year old lens. Note the vertical scale is seven times as large as the horizontal scale. The lens surface profile shown represents semi-elliptical fits to the coordinates of the surface pixels.

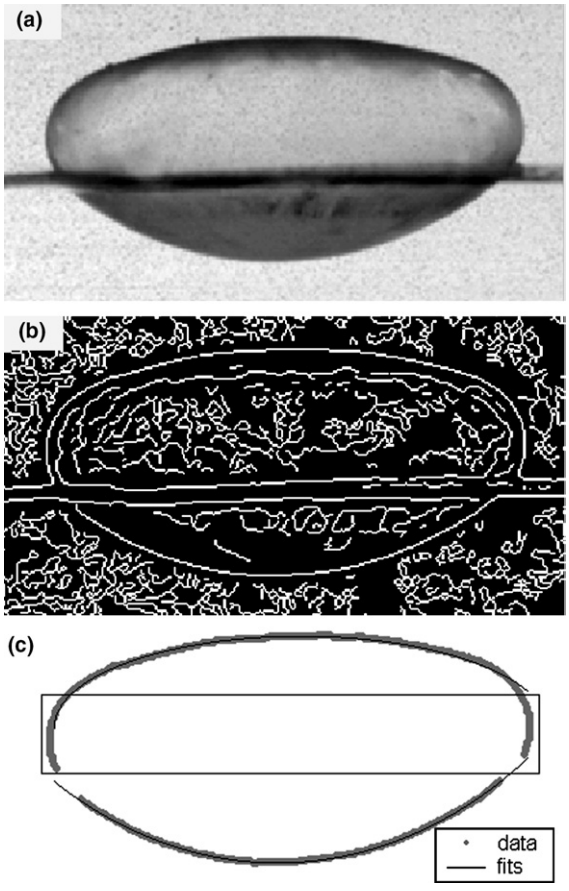

Fig. 9. Semi-elliptical fitting to the lens surfaces during a scanning laser experiment. (a) Digitally captured surface of the crystalline lens. (b) Binary image of the lens after edge detection employing the Canny method. (c) Semi-elliptical fits to the edge data.

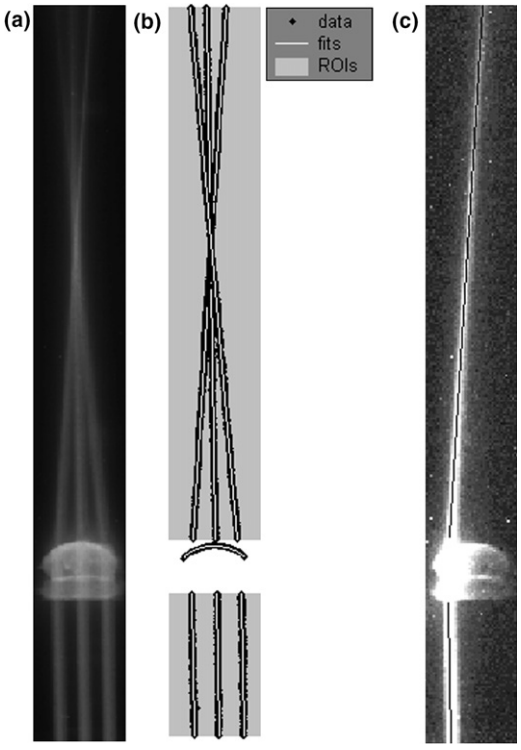

Fig. 10. Results from a scanning laser experiment. (a) An image constructed by superimposing the captured refraction of three laser beams. (b) Data points acquired using the threshold technique discussed in Section 2.3, together with linear fits to data corresponding to laser beams and the semi-elliptical front surface of lens. The grey shading indicates the regions of interest (ROIs) used to sample data for the laser beams. (c) Linear fit to an incident and refracted beam superimposed on its captured image. The contrast has been adjusted so that the beams and their fits can be viewed more clearly.

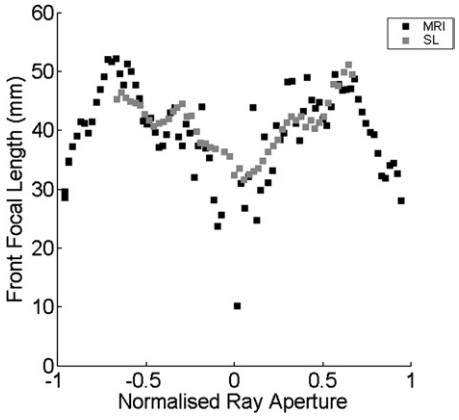

Fig. 11. Comparison of longitudinal aberration curves obtained from MRI and scanning laser (SL) experiments for a 35 year old lens.

3.3. Contributions of surface and GRIN refraction to paraxial power of the isolated lens

As discussed in Section 2.6, in order to measure lens power and determine the contribution of surface refraction, the simulated ray traces were re-performed in the

Table 1
Scanning laser and MRI estimates of front focal length (FFL) anterior and posterior vertex curvatures (C_a and C_p respectively), equatorial diameter (D) and thickness (T) of the human eye lens in vitro

Scanning laser	MRI
FFL = 34.9(±2.4) + 0.372(±0.048) × Age (R = 0.876, p < 0.0001)	FFL = 26.8(±3.5) + 0.459(±0.071) × Age (R = 0.837, p < 0.0001)
C_a = 0.163(±0.011) − 1.09(±0.22) × 10^{-3} × Age (R = −0.757, p < 0.0001)	C_a = 0.1363(±0.0015) − 6.9(±2.8) × 10^{-4} × Age (R = −0.535, p = 0.015)
C_p = −0.183(±0.011) + 6.1(±2.2) × 10^{-4} × Age (R = 0.537, p = 0.0146)	C_p = −0.1777(±0.0014) + 6.7(±3.0) × 10^{-4} × Age (R = 0.461, p = 0.0406)
D = 7.94(±0.13) + 2.03(±0.27) × 10^{-2} × Age (R = 0.873, p < 0.0001)	D = 8.14(±0.11) + 1.76(±0.23) × 10^{-2} × Age (R = 0.872, p < 0.0001)
T = 4.87(±0.16) + 3.26(±0.32) × 10^{-3} × Age (R = 0.024, p = 0.9206)	T = 4.77(±0.15) + 4.2(±3.1) × 10^{-3} × Age (R = 0.307, p = 0.188)

All dimensions are in mm and Age is in years.

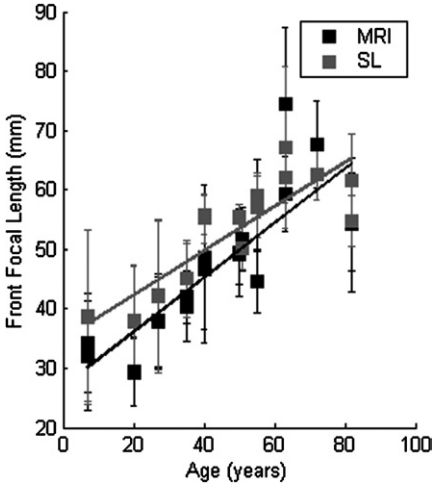

Fig. 12. Front focal lengths of isolated human lenses as a function of age, measured using the MRI technique (dark symbols) and the scanning laser (SL) apparatus, together with regression lines.

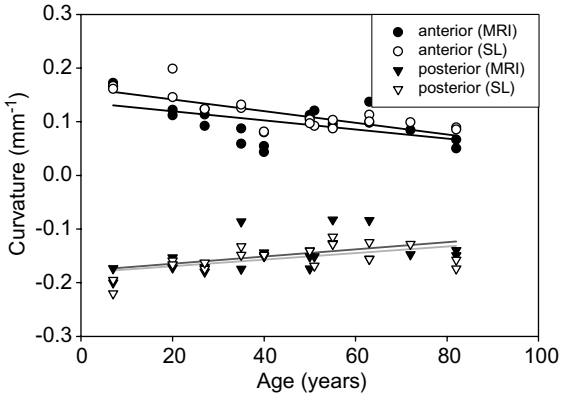

Fig. 13. Dependence of lens anterior and posterior vertex curvatures on age determined using the MRI and scanning laser (SL) experiments, together with regression lines.

standard way i.e. rays incident onto the anterior surface, focal length measured from the principal curve, and the lens surrounded by a medium with refractive index corresponding to in vivo conditions (1.336 according to the Gullstrand schematic eye). As before the intersection of the entrance and exit rays gave the principal points. An example of a principal curve fitted to Eq. (1) is illus-

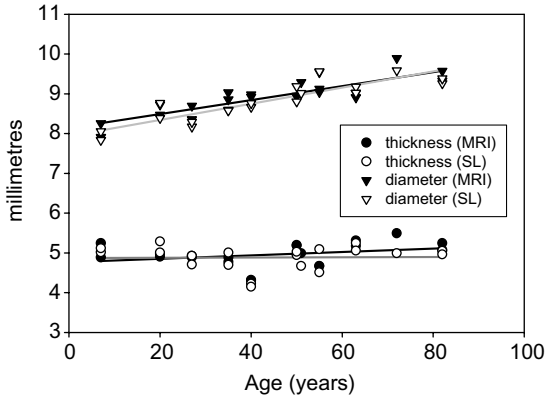

Fig. 14. Dependence of lens diameter and thickness on age determined from the MRI experiment and scanning laser (SL) experiments, together with regression lines.

trated in Fig. 15. Fig. 16 displays longitudinal aberration curves for young (7 years) and old (51 years) isolated lenses, together with fourth order even polynomial fits. As illustrated in this figure, young lenses tended to have short paraxial focal lengths that increase with ray aperture (negative longitudinal aberration). As the age of the lens increases the paraxial focal length tends to become longer than that for wider apertures (positive longitudinal aberration). This trend was also observed in previous studies of isolated lenses (Glasser & Campbell, 1998, 1999). Using the methods discussed in Section 2.6, total paraxial power, surface vertex power and total mean power were estimated. The age

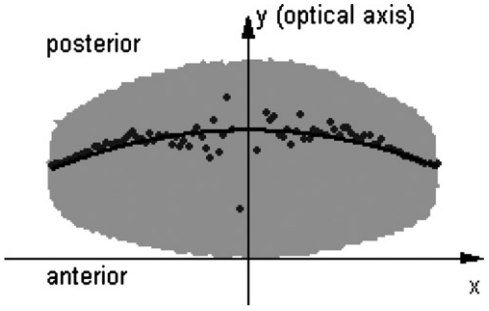

Fig. 15. Example of a principal curve (—) fitted to the principal points (●) of an isolated human lens (▬).

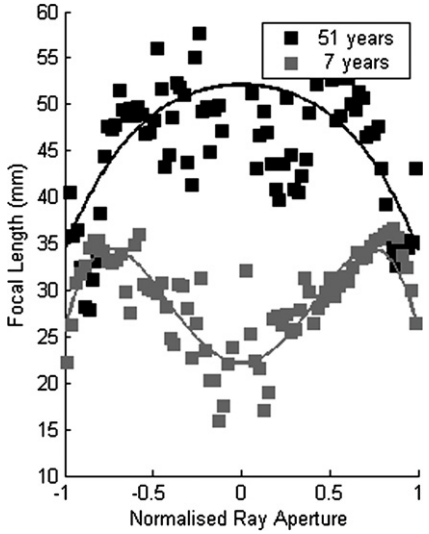

Fig. 16. Longitudinal aberration data for 51 (top) and 7 year old isolated human lenses, fitted to a fourth order even polynomial.

dependence in each case was fitted to a first order polynomial and found to be given by:

$$\text{total paraxial power} = 50.1(\pm 2.9) - 0.363(\pm 0.059) \times \text{Age} \quad (7)$$

($R = 0.822$, $p < 0.0001$),

$$\text{surface vertex power} = 10.87(\pm 0.76) - 0.052(\pm 0.016) \times \text{Age} \quad (8)$$

($R = 0.617$, $p = 0.0037$),

$$\text{total mean power} = 44.8(\pm 1.9) - 0.272(\pm 0.039) \times \text{Age} \quad (9)$$

($R = -0.852$, $p < 0.0001$),

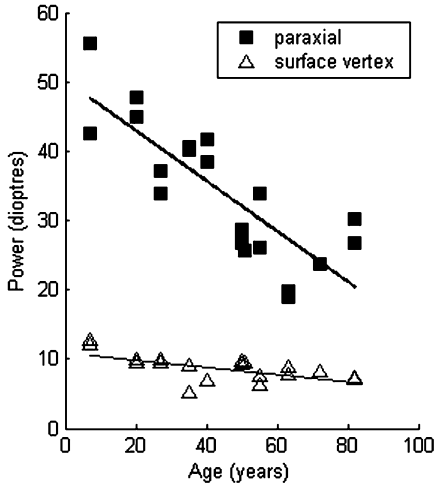

Fig. 17. Paraxial and surface vertex powers versus age for isolated human lenses.

where power is in dioptres and Age in years. The total paraxial power and surface vertex power data are plotted in Fig. 17, together with the regression results. A comparison of the paraxial power and surface vertex powers in Fig. 15 and Eqs. (7) and (8) reveals that as expected, surface refraction is only a minor contributor to total paraxial power, GRIN refraction being the major component of light refraction.

4. Discussion

The age-dependent trends in focal length measured using the MRI and scanning laser techniques (Fig. 12) were in good agreement. However we found that any decrease in central refractive index with age, as reported by Moffat et al. (2002a, 2002b), was not statistically significant. This may reflect the improved calibration of refractive index versus R_2 value (Fig. 2) employed in this study. In the 2002 study, the preliminary calibration curve consisting of only 7 data points was approximated by a linear fit. However from Fig. 2 it can be seen that the more accurate curve of this study (consisting of 30 data points) has negative curvature, i.e. the rate of increase in refractive index decreases with increasing R_2. Therefore the linear approximation of refractive index versus R_2 would tend to overestimate any decrease in central refractive index with age. Also, in order to accurately observe the underlying trend obscured by the wide individual variations displayed by humans, it may be necessary to perform a much larger study than those undertaken to date. In eye studies, it is not uncommon to examine over 100 subjects in order to establish the underlying trends in data displaying a large amount of scatter.

The most dramatic age-related trend in refractive index distribution that we observed was that the refractive index profiles became more flat in the central region with age, accompanied by a steepening of the profile, particularly in the equatorial periphery of the lens. This observation supports the explanation of the 'Lens Paradox' (the fact that the eye does not become myopic with age despite increased curvature of the lenticular surfaces) proposed by Smith, Pierscionek, and Atchison (1991) and Smith, Atchison, and Pierscionek (1992). Previously it has been concluded that the decrease in central refractive index with age is the sole mechanism behind the 'Lens Paradox' (Moffat et al., 2002a, 2002b). However the results of this study indicate that the mechanism may be twofold i.e. the changing shape of the refractive index profile accompanied perhaps by a small decrease in central refractive index.

While a formula has been developed for adjusting refractive indices of vertebrate crystalline lens tissues for different wavelengths of light (Kröger, 1992), it results in an uncertainty in refractive estimates almost

an order of magnitude larger than the uncertainty associated with the MRI technique. This formula was used in the previous study on porcine lenses (Jones & Pope, 2004) where the laser wavelength (543.5 nm) was significantly different to that detected by the Abbe refractometer (589 nm). However in this study the laser wavelength of 594 nm is very similar to that detectable by the Abbe refractometer and it was not deemed necessary to correct the resulting refractive index map.

In the scanning laser experiments, we were unable to obtain the longitudinal aberration curve for the full diameter of the lens because the equatorial periphery was obscured by the pedestal which was used to support it (see Fig. 1). It is for this reason that the scanning laser data in Fig. 11 span a more limited range of apertures than the MRI data. In some cases there was also a sharp discontinuity in the central region of the longitudinal aberration curve obtained from the scanning laser experiments, due to compounding of the errors associated with slight misalignment of the incident laser beam with the optical axis of the lens and amplification of the corresponding errors in the estimated focal length because the exit beam is almost parallel with the optical axis in this region.

In this study we have examined the refractive index distribution and optical properties of the isolated human lens. When the lens is excised from the eye, the zonular tension is completely removed and the lens takes on its most accommodated state. Whether the level of accommodation of the excised lens is equal to or greater than that of the fully accommodated lens in vivo is not clear. Brown (1974b) observed that the zonular fibres ran a "relaxed, sinuous course" in a young eye where accommodation was induced pharmacologically. In a study where isolated lenses were mechanically stretched to mimic 'unaccommodation', Glasser and Campbell (1998) were able to decrease the mean power of the lens by an amount similar to the accommodative amplitude measured using a subjective technique (Koretz, Kaufman, Neider, & Goeckner, 1989; Ungerer, 1986). However it is known that this subjective method overestimates accommodative amplitude by approximately 2 dioptres due to depth of field effects. Further, during accommodation the eye increases power by a reduction in distance between the posterior corneal surface and the anterior lens surface (Koretz, Cook, & Kaufman, 2002) as well as an increase in lens power, so that we would expect the increase in lenticular power to be less than the increase in the power of the eye. In their previous study (Glasser & Campbell, 1998), focal lengths were measured using a scanning laser apparatus similar to our own, and the maximum decrease in mean focal length obtained with stretching versus age of the lens was fitted to a fifth order polynomial. The resulting regression equation indicated that no change in focal length occurred with stretching as the age of the lens reached about 60 years. In the present study the power of the isolated lens was found to decrease with age (as expected). We were interested to see whether or not the observed age-related decrease in power was due solely to the different accommodative states of the lenses. The mean power of the 60 year old lens of this study was estimated by evaluating Eq. (9) for Age = 60. This value was then subtracted from the measured mean powers of each of the lenses whose age was less than 60 years. These data points were then plotted together with the fifth order polynomial of Glasser and Campbell (1998) for comparison (Fig. 18). (Although this previous study used a different wavelength of light, 633 nm compared to 589 nm that the refractive index maps of this study correspond to, the differences are not large and it is the change in power, rather than absolute values of power that we are concerned with here). The results indicate that the age-related decrease in the power of the isolated lens is due entirely to the reduction in accommodative state that is obtained upon removal of zonular tension when the lens is excised from the eye. This result was expected because the power of the unaccommodated lens is generally assumed to be age-independent (see e.g. Atchison & Smith, 2000).

In the unaccommodated eye both the anterior and posterior surface curvatures have been found to increase with age (Brown, 1974a; Dubbelman & van der Heijde, 2001; Koretz, Cook, & Kaufman, 2001), while the diameter has been reported to remain constant with age in adulthood (Strenk et al., 1999), and the sagittal thickness to increase with age (Cook, Koretz, Pfahnl, Hyun, & Kaufman, 1994; Dubbelman, van der Heijde, & Weeber, 2001; Strenk et al., 1999). Different trends were observed in this study of the isolated lens because, upon

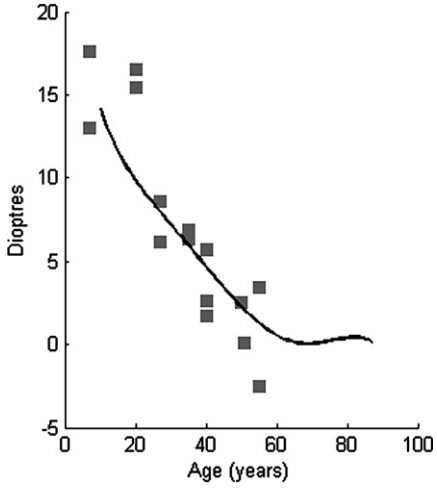

Fig. 18. Mean power minus the corresponding mean power at 60 years found in this study (■), compared with a fifth order polynomial fit to data describing the maximum decrease in mean power of isolated lenses with mechanical stretching measured by Glasser and Campbell (1998) (—).

removal of zonular tension with excision from the eye, the younger lenses assume a greater level of accommodation. As a result, for isolated lenses, the age-related trend in vertex curvatures is reversed, an age-related increase in diameter is observed, and the increase in lens thickness with age is not as pronounced as is observed in vivo (Figs. 13 and 14, Table 1). From Fig. 17 it can be seen that due to the decreasing vertex curvatures with age, the surface power of the isolated lens also decreases. However, this decrease only partially accounts for the decrease in total paraxial power. Further by comparing the plots for paraxial power and surface vertex power in Fig. 17, it can be seen that surface refraction is the minor component of focal power in the isolated lens, GRIN refraction being the main mechanism by which the crystalline lens focuses light.

From Fig. 17 it can also be seen that the paraxial power of these isolated lenses appears to be higher than that measured in vivo, even in the fully accommodated eye. For example, the power of the lens in the relaxed eye is around 19 dioptres (Atchison & Smith, 2000). A 20 year old subject has accommodative amplitude of around 8–10 dioptres which decreases linearly with age to zero dioptres at around 50–60 years of age (Koretz et al., 1989). Possible reasons for the discrepancies are (1) upon removal of zonular tension when excised from the eye, the lens becomes more accommodated than it is capable of in vivo; and (2) to achieve a given increase in accommodation, the lens power must change by a greater amount than the measured accommodation amplitude of the eye as a whole. As an example, for the Gullstrand number 1 schematic eye an amplitude of accommodation of 10.9D is achieved by an increase in lens power of 13.9D (Atchison & Smith, 2000).

Figs. 5 and 6 illustrate that as the age of the lens increases, the refractive index profile flattens in the central region and the index gradient steepens, especially in the equatorial periphery of the lens. This index distribution was found to be quite complex and was not very well approximated by any of the standard elliptical lens or bi-elliptical models (Smith et al., 1991; Smith et al., 1992). Detailed modelling of the refractive index distribution and its age-dependence will be the subject of a future article. Smith et al. (1992) proposed a simple age-dependent model of index distribution to explain why the eye does not become myopic with age despite increased lenticular surface curvatures (the Lens Paradox). In these models they described the index distribution of the crystalline lens as a single function of normal distance from the lens centre. One of these functions took the form:

$$N(r) = c_0 + c_p r^p \tag{10}$$

where N is refractive index, r is the normalised distance from lens centre (e.g. $r = 0$ at the centre, $r = 1$ at the surface of the lens), c_0 and c_p are coefficients stipulating the centre and surface refractive indices of the lens, and p is the coefficient that describes how the value of refractive index changes from the centre to the surface of the lens. Some examples of how the p-coefficient affects the index profiles are shown in Fig. 19(a). Low values of the p-coefficient correspond to curved profiles, as was observed for the young isolated lenses, while high values of the p-coefficient correspond to profiles that are flat in the central region accompanied by a steep gradient in the equatorial periphery, as was observed for the older isolated lenses. Fig. 19(b) displays the longitudinal aberration curves obtained from ray traces through an elliptical lens where all parameters are kept fixed apart from a variable p-coefficient. Qualitatively, the curves are similar to those observed for the isolated lenses of this study, (examples of which are shown in Fig. 16). Low values of the p-coefficient (indicating curved index profiles as observed for young lenses) correspond to

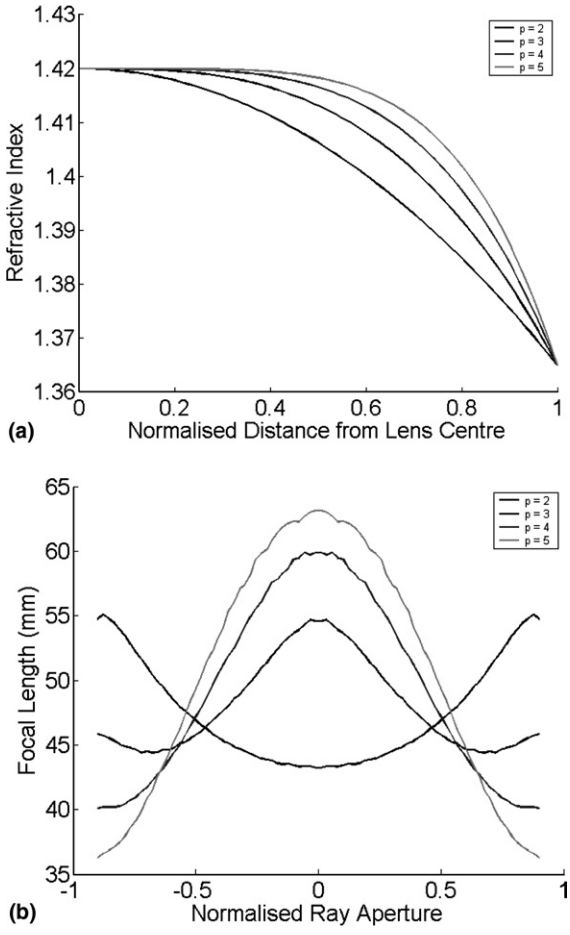

Fig. 19. Dependence of (a) refractive index profile and (b) longitudinal aberration curve on the p-coefficient of Eq. (9). Simulated ray traces were performed through an elliptical lens of minor axis 2.25 mm (corresponding to a thickness of 4.5 mm) and major axis 4.5 mm (corresponding to a diameter of 9 mm). The central index of the lens was 1.42, the surface index was 1.37, and the surrounding medium had an index of 1.34.

short paraxial focal length (high paraxial power) and negative longitudinal aberration, while high values of the *p*-coefficient (indicating flat index profiles as observed for old lenses) correspond to high paraxial focal length (low paraxial power) and positive longitudinal aberration. Therefore we conclude that this observed age-related change in the index profile of isolated human lenses is an important mechanism underlying the observed change in the power and longitudinal aberration of the crystalline lens. While we found that individual index profiles could be described by Eq. (10), we found that the *p*-coefficient varied with the angular orientation of the profile, so that we could not describe the index distribution of the entire lens by a single function of normalised distance from the lens centre. The deviation of the human crystalline lens from this simple model is a probable cause for Pierscionek et al's (1988) inability to correctly predict the exit angles of laser beams in their model-dependent refractive index measurements of human lenses.

While this study has provided valuable insights into the mechanisms behind the age-related changes in the optical properties of the isolated crystalline lens, it also highlights the need for reliable, model-independent, in vivo measurements of refractive index distribution.

5. Conclusions

Agreement between lens focal lengths measured using the two independent methods employed in this study verifies that accurate refractive index maps can be obtained using the MRI technique. We found that a gradual flattening of the index profile in the central region of the lens, accompanied by a steepening of the profile in the equatorial periphery, (combined perhaps with a small decrease in central refractive index), is the main mechanism underlying the observed age-dependent changes in the optical properties of the isolated lens.

Acknowledgment

The authors wish to thank Queensland Eye Bank for supply of human eye lenses.

References

Acosta, E., Flores, R., Vázquez, D., Ríos, S., Garner, L., & Smith, G. (2002). Tomographic method for measurement of the refractive index profile of optical fibre preforms and rod GRIN lenses. *Japanese Journal of Applied Physics, 41*, 4821–4824.

Al-Ahdali, I., & Messiery, E. (1995). Examination of the effect of the fibrous structure of a lens on the optical characteristics of the human eye: A computer-simulated model. *Applied Optics, 34*, 5738–5745.

Artal, P., Berrio, E., Guirao, A., & Piers, P. (2002). Contribution of the cornea and internal surfaces to the change of ocular aberrations with age. *Journal of the Optical Society of America A, 19*, 137–143.

Atchison, D. A., & Smith, G. (1995). Continuous gradient index and shell models of the human lens. *Vision Research, 35*, 2529–2538.

Atchison, D. A., & Smith, G. (2000). *Optics of the human eye*. Oxford: Butterworth-Heinemann.

Barrell, K. F., & Pask, C. (1978). Nondestructive index profile measurement on noncircular optical fibre preforms. *Optics Communications, 27*, 230–234.

Barbero, S., Glasser, A., Clark, C., & Marcos, S. (2004). Accuracy and possibilities for evaluating the lens gradient-index using a ray tracing tomography global optimization strategy. *Investigative Ophthalmology and Visual Science, 45*, ARVO E-Abstract 1723.

Brown, N. (1974a). The shape of the lens equator. *Experimental Eye Research, 19*, 571–576.

Brown, N. (1974b). The change in lens curvature with age. *Experimental Eye Research, 19*, 175–183.

Campbell, M. C. W. (1984). Measurement of refractive index in an intact crystalline lens. *Vision Research, 24*, 409–415.

Carr, H. Y., & Purcell, E. M. (1954). Effects of diffusion on free precession in nuclear magnetic resonance experiments. *Physical Review, 94*, 630–638.

Chan, D. Y., Ennis, J. P., Pierscionek, B. K., & Smith, G. (1988). Determination and modelling of the 3-gradient refractive indices in crystalline lenses. *Applied Optics, 27*, 926–931.

Cheng, H., Barnett, J. K., Vilupuru, A. S, Marsack, J. D., Kasthurirangan, S., Applegate, R. A., et al. (2004). A population study on changes in wave aberrations with accommodation. *Journal of Vision, 4*, 272–280.

Chu, P. L. (1977). Nondestructive measurement of index profile of an optical fibre preform. *Electronics Letters, 13*, 736–738.

Cook, C. A., Koretz, J. F., Pfahnl, A., Hyun, J., & Kaufman, P. L. (1994). Aging of the human crystalline lens and anterior segment. *Vision Research, 34*, 2945–2954.

Dubbelman, M., & van der Heijde, G. L. (2001). The shape of the aging human lens: Curvature, equivalent refractive index and the lens paradox. *Vision Research, 41*, 1867–1877.

Dubbelman, M., van der Heijde, G. L., & Weeber, H. A. (2001). The thickness of the aging human lens obtained from corrected Scheimpflug images. *Optometry and Vision Science, 78*, 411–416.

Fagerholm, P. P., Philipson, B. T., & Lindström, B. (1981). Normal human lens, the distribution of protein. *Experimental Eye Research, 33*, 615–620.

Glasser, A., & Campbell, M. C. W. (1998). Presbyopia and the optical changes in the human crystalline lens with age. *Vision Research, 38*, 209–229.

Glasser, A., & Campbell, M. C. W. (1999). Biometric, optical and physical changes in the isolated human crystalline lens with age in relation to presbyopia. *Vision Research, 39*, 1991–2015.

Jones, C. E., & Pope, J. M. (2004). Measuring optical properties of an eye lens using magnetic resonance imaging. *Magnetic Resonance Imaging, 22*, 211–220.

Koretz, J. F., Cook, C. A., & Kaufman, P. L. (2001). Aging of the human lens: Changes in lens shape at zero-diopter accommodation. *Journal of the Optical Society of America A, 18*, 265–272.

Koretz, J. F., Cook, C. A., & Kaufman, P. L. (2002). Aging of the human lens: Changes in lens shape upon accommodation and with accommodative loss. *Journal of the Optical Society of America A, 19*, 144–151.

Koretz, J. F., Kaufman, P. L., Neider, M. W., & Goeckner, P. A. (1989). Accommodation and presbyopia in the human eye—aging of the anterior segment. *Vision Research, 29*, 1685–1692.

Kröger, R. H. H. (1992). Methods to estimate dispersion in vertebrate ocular media. *Journal of the Optical Society of America A, 9*, 1486–1490.

Matthiessen, L. (1880). Untersuchungen ueber den Aplanatismus und die Periscopie der Krystallinsen in den Augen der Fische. *Pfluegers Arch. Physiol., 21*, 287–307, cited in Pierscionek, B. K., & Chan, D. Y. C. (1989). Refractive index gradient of human lenses. *Optometry and Vision Science, 66*, 822–829.

Meiboom, S., & Gill, D. (1958). Modified spin-echo method for measuring nuclear relaxation times. *The Review of Scientific Instruments, 29*, 688–691.

Moffat, B. A., Atchison, D. A., & Pope, J. M. (2002a). Age-related changes in refractive index distribution and power of the human lens as measured by magnetic resonance micro-imaging in vitro. *Vision Research, 42*, 1683–1693.

Moffat, B. A., Atchison, D. A., & Pope, J. M. (2002b). Explanation of the lens paradox. *Optometry and Vision Science, 79*, 148–150.

Nakao, S., Fujimoto, S., Nagata, R., & Iwata, K. (1968). Model of refractive-index distribution in the rabbit crystalline lens. *Journal of the Optical Society of America, 58*, 1125–1130.

Pierscionek, B. K. (1997). Refractive index contours in the human lens. *Experimental Eye Research, 64*, 887–893.

Pierscionek, B. K., Chan, D. Y. C., Ennis, J. P., Smith, G., & Augusteyn, R. C. (1988). Nondestructive method of constructing three dimension gradient index models for crystalline lenses: 1. Theory and experiment. *American Journal of Optometry and Physiological Optics, 65*, 481–491.

Pomerantzeff, O., Pankratov, M., Wang, G.-J., & Dufault, P. (1984). Wide-angle optical mode of the eye. *American Journal of Optometry and Physiological Optics, 61*, 166–176.

Roth, E. H., & Kluxen, G. (1990). In vivo measurements of the distribution of the refractive index of the human lens with a Scheimpflug's procedure on the anterior segment of the eye and a He–Ne laser beam. *Fortschritte der Opthalmologie, 87*, 312–316.

Sharma, A., Kumar, D. V., & Ghatak, A. K. (1982). Tracing rays through graded-index media: A new method. *Applied Optics, 21*, 984–987.

Smith, G., Atchison, D. A., & Pierscionek, B. K. (1992). Modeling the power of the aging human eye. *Journal of the Optical Society of America A, 9*, 2111–2116.

Smith, G., Cox, M. J., Calver, R., & Garner, L. F. (2001). The spherical aberration of the crystalline lens of the human eye. *Vision Research, 41*, 235–243.

Smith, G., Pierscionek, B. K., & Atchison, D. A. (1991). The optical modelling of the human lens. *Ophthalmolic and Physiological Optics, 11*, 359–369.

Strenk, S. A., Semmlow, J. L., Strenk, L. M., Munoz, P., Gronlund-Jacob, J., & DeMarco, J. K. (1999). Age-related changes in human ciliary muscle and lens: A magnetic resonance imaging study. *Investigative Ophthalmology and Visual Science, 40*, 1162–1169.

Ungerer, J. (1986). The optometric management of presbyopic airline pilots. Unpublished MSc Optometry thesis, University of Melbourne, cited in Atchison and Smith (2000).

Vilupuru, A. S., & Glasser, A. (2001). Optical and biometric relationships of the isolated pig crystalline lens. *Ophthalmolic and Physiological Optics, 21*, 296–311.

Zar, J. H. (1984). *Biostatistical analysis*. New Jersey: Prentice-Hall, pp. 360–366.